Solar Phys (2011) 268: 213–230
DOI 10.1007/s11207-010-9674-5

Determining the Solar Source of a Magnetic Cloud Using a Velocity Difference Technique

L.K. Harra · C.H. Mandrini · S. Dasso · A.M. Gulisano · K. Steed · S. Imada

Received: 31 August 2010 / Accepted: 4 November 2010 / Published online: 7 December 2010

Abstract For large eruptions on the Sun, it is often a problem that the core dimming region cannot be observed due to the bright emission from the flare itself. However, spectroscopic data can provide the missing information through the measurement of Doppler velocities. In this paper we analyse the well-studied flare and coronal mass ejection that erupted on the Sun on 13 December 2006 and reached the Earth on 14 December 2006. In this example, although the imaging data were saturated at the flare site itself, by using velocity measurements we could extract information on the core dimming region, as well as on remote dimmings. The purpose of this paper is to determine more accurately the magnetic flux of the solar source region, potentially involved in the ejection, through a new technique. The results of its application are compared to the flux in the magnetic cloud observed at 1 AU, as a way to check the reliability of this technique. We analysed data from the *Hinode* EUV Imaging Spectrometer to estimate the Doppler velocity in the active region and its surroundings before and after the event. This allowed us to determine a Doppler velocity 'difference' image. We used the velocity difference image overlayed on a Michelson Doppler Imager magnetogram to identify the regions in which the blue shifts were more prominent after

L.K. Harra (✉) · K. Steed
UCL—Mullard Space Science Laboratory, Holmbury St. Mary, Dorking, Surrey, RH5 6NT, UK
e-mail: lkh@mssl.ucl.ac.uk

C.H. Mandrini · S. Dasso · A.M. Gulisano
Instituto de Astronomía y Física del Espacio, CONICET-UBA, 1428 Buenos Aires, Argentina

C.H. Mandrini
e-mail: mandrini@iafe.uba.ar

C.H. Mandrini · S. Dasso · A.M. Gulisano
Facultad de Ciencias Exactas y Naturales, FCEN, UBA, CC. 67, Suc. 28, 1428 Buenos Aires, Argentina

S. Dasso
Departamento de Física, FCEN, UBA, Buenos Aires, Argentina

S. Imada
Institute of Space and Astronautical Science, Japan Aerospace Exploration Agency, 3-1-1 Yoshinodai, Sagamihara-shi, Kanagawa 229-8510, Japan

the event; the magnetic flux in these regions was used as a proxy for the ejected flux and compared to the magnetic cloud flux. This new method provides a more accurate flux determination in the solar source region.

Keywords Coronal mass ejections: interplanetary · Coronal mass ejections: low coronal signatures

1. Introduction

Coronal mass ejections (CMEs) are intricately linked to space weather events and storms; hence it is of critical importance to understand their trigger, origin, and propagation through the heliosphere. CMEs are most easily observed using coronagraph data where the solar disk is blocked out. However, the source of a CME can only be determined using solar disk data, from which it is more difficult to identify CMEs. On-disk signatures studied over the years are summarised by Hudson and Cliver (2001). Coronal 'dimmings' are one of the main on-disk signatures of a CME. When originally discovered during the *Skylab* era, they were known as transient coronal holes (*e.g.* Rust, 1983). Coronal dimming characteristics suggest they are due to a reduction of coronal plasma following an eruption (Hudson, Acton, and Freeland, 1996). Sterling and Hudson (1997) showed a very clear example of dimmings that persisted for three days following a flare and related halo CME, using data from the Soft X-ray Telescope (SXT) on board *Yohkoh*. They suggested that the dimmings were consistent with the source of the CME being a flux rope that erupted, leaving behind the dimming regions. Similar behaviour has also been observed in the Extreme Ultraviolet Imaging Telescope (EIT, Delaboudinière *et al.*, 1995) data on board the *Solar and Heliospheric Observatory* (SOHO) (*e.g.* Thompson *et al.*, 1998). Estimates suggest that these regions could contribute $\geq$ 50% of the total mass of the CME (*e.g.* Zhukov and Auchère, 2004; Sterling and Hudson, 1997; Harrison and Lyons, 2000).

Dimmings are an extremely important diagnostic for understanding CMEs. Recent work by Reinard and Biesecker (2009) has demonstrated that CMEs with associated dimmings have higher speeds than those without obvious dimmings. The events without dimmings do not reach speeds higher than the fast solar wind speed.

Dimmings are often present on both sides of an erupting configuration. It has been suggested that these dimmings mark the position of the ejected flux rope footpoints (Sterling and Hudson, 1997; Webb *et al.*, 2000). In this context, the eruption of a magnetic flux rope forms the core magnetic field of the CME, which is later observed as an interplanetary CME (ICME) or magnetic cloud (MC). Then, the magnetic flux in the dimming regions could be used as a proxy of the ejected flux at the Sun and be compared to the flux in the associated ICME or MC. Attrill *et al.* (2006) and Crooker and Webb (2006) studied the simple case of the 12 May 1997 event and found that, although there were two dimming regions consistent with the idea of an erupting flux rope, one of these regions suffered interchange reconnection with a coronal hole which changed its magnetic structure. This example demonstrates that, even in the simplest case, large-scale magnetic interactions are always possible that can confuse our understanding of the magnetic structure of the subsequent ICME. Furthermore, in large-scale and energetic events, which expand strongly and interact with the magnetic field of the surroundings, the interpretation of dimmings requires a careful analysis of the global magnetic configuration. A fraction of the dimmed regions could be formed by reconnection between the erupting field and other magnetic structures via a step-like process

(Attrill *et al.*, 2007). This process may encompass not only the neighbouring regions but others located farther away, giving origin to multiple dimmed zones or secondary dimmings (see *e.g.* Mandrini *et al.*, 2007). On the other hand, and in the context of the flux rope interpretation, the extremely bright emission at the flare site would cover the two main or core dimmings. These, in general, have the highest magnetic flux (since part of them lie on the *active region* (AR)); thus, the estimation of the flux involved in the ejection would not be reliable.

The launch of *Hinode* in 2006 provided the ability to measure the properties of dimmings in a different way, using the EUV Imaging Spectrometer (EIS, Culhane *et al.*, 2007). The first cases analysed were the flares and CMEs of 13 and 14 December 2006 by Harra *et al.* (2007) and Imada *et al.* (2007). Harra *et al.* (2007) showed that the dimming region has a clear structure with extended loops whose footpoints are the source of the strongest outflow at speeds of 40 km s^{-1}. This confirms that the loops that were disrupted during the event do lose plasma and hence are likely to form part of the CME. This is the first time that the velocity of the coronal plasma was measured in an extended dimming region away from the flare. In addition, there was a weaker steady outflow from extended, faint loops outside the AR before the eruption, which was also long lasting. Imada *et al.* (2007) analysed the flare of 13 December 2006 and found a temperature dependence of the outflows – the hotter the plasma, the faster it flowed. Jin *et al.* (2009) have analysed both of these December 2006 events and found that the velocity also correlates with the photospheric magnetic field. They found that the mass loss determined from the dimming regions was smaller than that derived from white-light observations.

Möstl *et al.* (2008) have made use of data from the *Advanced Composition Explorer* (ACE, Stone *et al.*, 1998) and *Wind* (Ogilvie and Desch, 1997) to reconstruct an MC. They have computed its magnetic flux and compared this value with that of the solar source identified in SOHO and *Transition Region and Coronal Explorer* (TRACE, Handy *et al.*, 1999) data. They found that the poloidal flux in the MC was similar to the reconnection flux of the flare, while the axial flux of the MC was an order of magnitude lower. This result is consistent with other works carried out by Longcope *et al.* (2007) and Qiu *et al.* (2007). Similar results were first found by Mandrini *et al.* (2005) and Attrill *et al.* (2006), using the flux in dimmed regions. Such information is invaluable in distinguishing between different CME initiation models (see the discussion in Mandrini *et al.*, 2009 and Mandrini, 2010).

On 13 December 2006 a flare and CME occurred in AR 10930. The flare started at 02:14 UT and reached *Geostationary Operational Environmental Satellite* (GOES) X-ray class X3.4. The activity in AR 10930 has been studied in great detail by several authors. Asai *et al.* (2008) studied strongly blue-shifted phenomena during this flare, finding two separate sources. The first was associated with a plasmoid ejection, and was observed across all temperature lines, reaching speeds of 250 km s^{-1}. The second phenomenon was only observed in the hot Fe XV and Ca XVII lines, and had a velocity of 450 km s^{-1}. These blue shifts were interpreted as being due to a magnetohydrodynamic (MHD) fast-mode shock wave. The filament was studied by Williams *et al.* (2009). They found that there were antisymmetric flows about the filament length, strongly suggestive of rotation before the flare impulsive phase. This is consistent with expansion of a twisted flux rope due to MHD helical kink instability. The coronal dimmings from this eruption and the one that followed were analysed in further detail by Attrill *et al.* (2010). The velocity in the dimming regions showed a gradual reduction in time, which was consistent with the recovery in intensity.

Liu *et al.* (2008) studied the 13 December 2006 CME from the Sun to interplanetary space. They measured the CME shock extent by using data from both the Earth and Ulysses and found it to be the largest shock extent ever detected. This work uses a technique that

combines MHD propagation of the solar wind and type II emissions to predict the shock arrival time at Earth.

In this paper we will analyse the CME on 13 December 2006, emphasising the determination of the magnetic flux involved in the ejection. Our aim is to develop a method that allows us to compute this flux, as accurately as possible, in cases in which the intensity of the flare emission covers the core dimmings. We will also model the MC associated with the ejection, estimate its magnetic flux, and compare it to our solar flux determination, as a way to check the reliability of our method. In Section 2 we briefly describe the data used. Section 3.1 presents the method and the results of its application. Section 3.2 discusses the probable origin of the remote dimmings observed to the east of AR 10930; in Section 3.3 we estimate the flux involved in the ejection. The MC model and its magnetic flux computation are described in Section 4.1, followed by a discussion about the comparison of fluxes at the solar and interplanetary levels in relation to the CME initiation process in Section 4.2. We discuss our findings in Section 5.

2. The Observations

The flare occurred on 13 December starting at 02:14 UT, reaching X3.4 on the GOES X-ray scale. AR 10930 has been studied in great detail. It consisted of a sunspot group with a newly emerged sunspot that showed rotation as it emerged, creating a high level of shear.

For this study, we predominantly used EIS data on board *Hinode*. The EIS instrument observes in two wavebands: 170 – 210 Å and 270 – 290 Å. It has four slit/slot positions: 1″, 2″, 40″, and 266″, allowing a wide choice of modes of operation. In this paper we will concentrate on data taken with the 1″ slit and using the fine mirror movement to 'raster' and build up an image. We analysed EIS data from the pre-flare phase, during the flare, and from the post-flare phase to track the changes in the velocity data, in particular. The pre-flare raster started at 20:51 UT on 12 December, the flare raster at 01:39 UT on 13 December, and the post-flare raster at 11:15 UT on 13 December. For each raster we followed the standard calibration procedure using the *eis_prep* routine in SolarSoft (Freeland and Handy, 1998). The slit tilt and orbital variation of the line position were removed. We concentrated on the strongest emission line Fe XII at 195.12 Å ($\log T = 6.1$). Each spectrum was fitted with a Gaussian profile, and the line width and Doppler velocity were determined. In cases where there was clearly more than one component in the profile, we used a double component fitting.

The X-Ray Telescope (XRT, Golub *et al.*, 2007) on *Hinode* was used to identify the coronal loops rooted in the AR before the flare, in particular, those taken with the thin beryllium filter.

For difference images we made use of the EIT on SOHO. We used the EIT images in CME watch mode taken through the 195 Å filter. The EIT data have a cadence of 12 min and a resolution of 5.2″. We used difference images for our analysis, which required that differential rotation be taken into consideration before subtraction.

To obtain the magnetograms we used the Michelson Doppler Imager (MDI, Scherrer *et al.*, 1995) on board SOHO. We used the full-disk level 1.5 magnetograms. They are constructed once every 96 min. The error in the flux densities per pixel in the averaged magnetograms is 9 gauss (G), and each pixel has a mean area of 1.96 Mm^2.

The alignment between the remote sensing instruments was carried out by aligning MDI and EIT and then EIT 195 Å with EIS 195 Å images. The MDI images had to be shifted by 20″ in both the x and y directions.

The *in situ* data analysed here were obtained by the Solar Wind Electron Proton Alpha Monitor (SWEPAM, McComas *et al.*, 1998) and by the Magnetic Field Experiment (MAG, Smith *et al.*, 1998), both on board ACE. The original magnetic field vector data are in geocentric solar ecliptic (GSE) coordinates.

3. The Magnetic Flux Ejected from the Sun

3.1. The Method

In order to determine the source of the CME, both within and outside the flaring region, we analysed the velocity maps before and during the flare. Figure 1 shows the intensity and Figure 2 shows the velocity maps determined from the EIS before and after the flare. The dramatic changes induced by the flare are very apparent in the intensity data. The core of

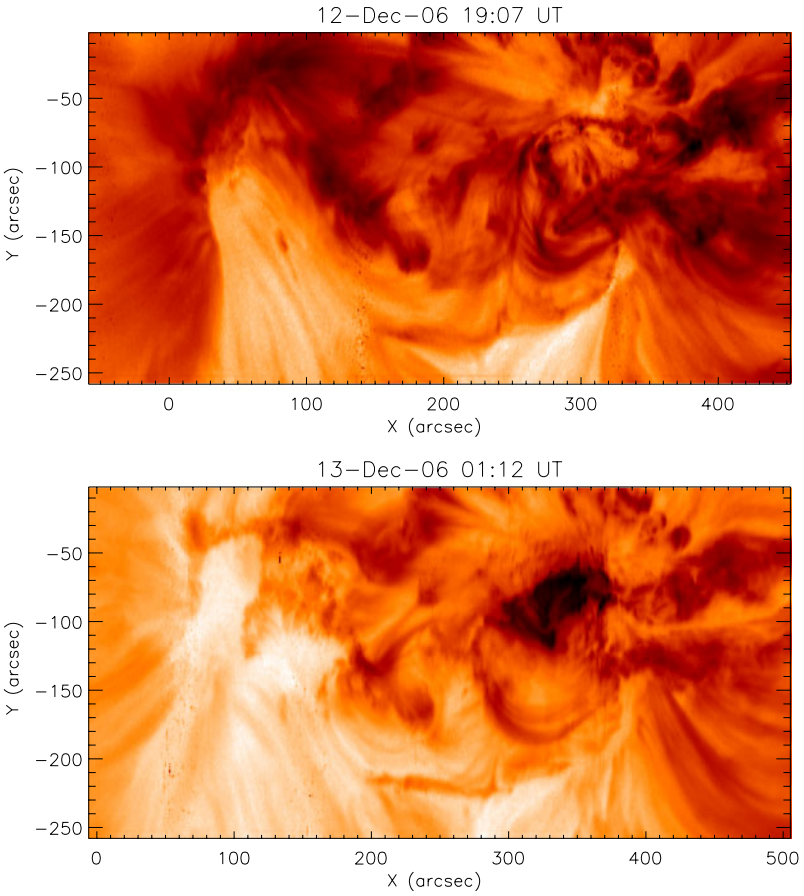

Figure 1 The intensity map in Fe XII before the large flare and CME on 13 December 2006 (top figure) and after the event (bottom figure). The intensity is in logarithmic scale. The flare core is centred on $(350'', -60'')$. The dimming region in the plage is centred on $100''$ in the x direction, and is widespread in the y direction. The times shown indicate the start of the EIS raster.

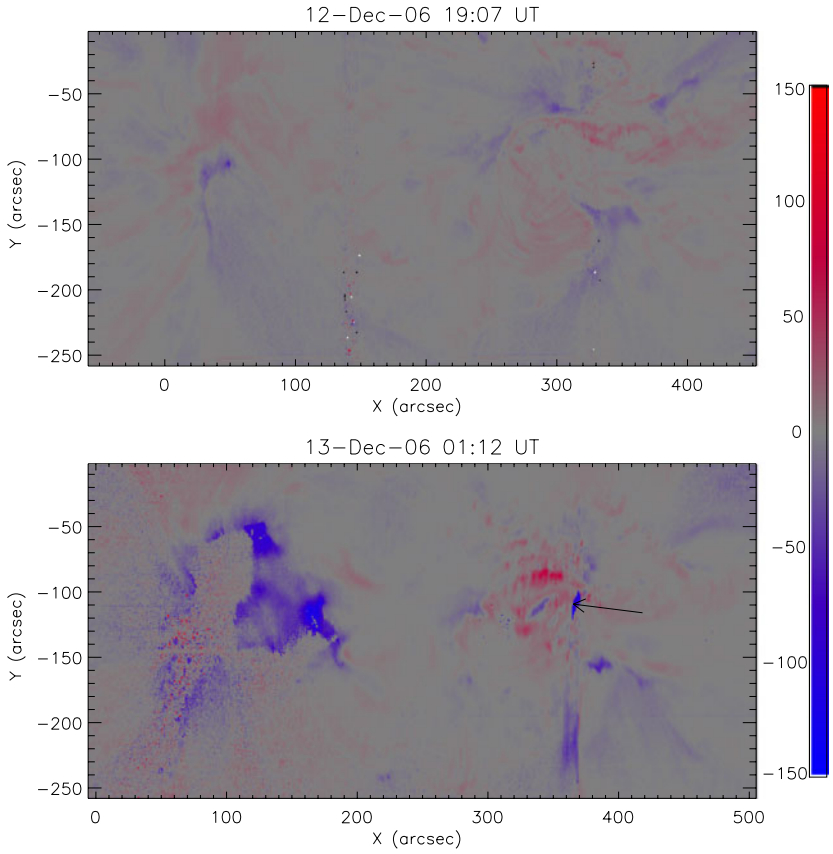

Figure 2 The Doppler velocity map in Fe XII before the large flare and CME on 13 December 2006 (top figure) and after the event (bottom figure). The velocity range is between ± 150 km s^{-1}, which is illustrated by the colour bar. The arrow shows where the filament eruption occurs, seen clearly in the velocity data. The times shown indicate the start of the EIS raster.

the AR in the flare map is very intense, and the surrounding region to the left shows a large reduction in intensity. There are strong blue shifts observed both in the core AR and in the plage region to the east.

Figure 3 shows the GOES light curve for context and examples of the line profiles in the dimming area of the plage region and in the core flare region, where the filament eruption occurs. The dimming region shows simple blue-shifted line profiles, whereas the flare region shows strong two-component profiles with a blue-shifted component with speeds reaching over 200 km s^{-1}. This occurs at the filament eruption region.

Figure 4 (top) shows the EIT dimming region determined from taking a difference image. The dark regions show the zones were the flux has been reduced in intensity due to the flare and eruption. The largest dimming region to the left is consistent with the strong outflow region shown in Figure 2 in the plage region. However, the main flare region is saturated and does not provide evidence of the eruption.

In order to determine the region in the flare core that contributed to the CME, we took a velocity difference image, which is shown in Figure 5. In order to do this, the flare raster was

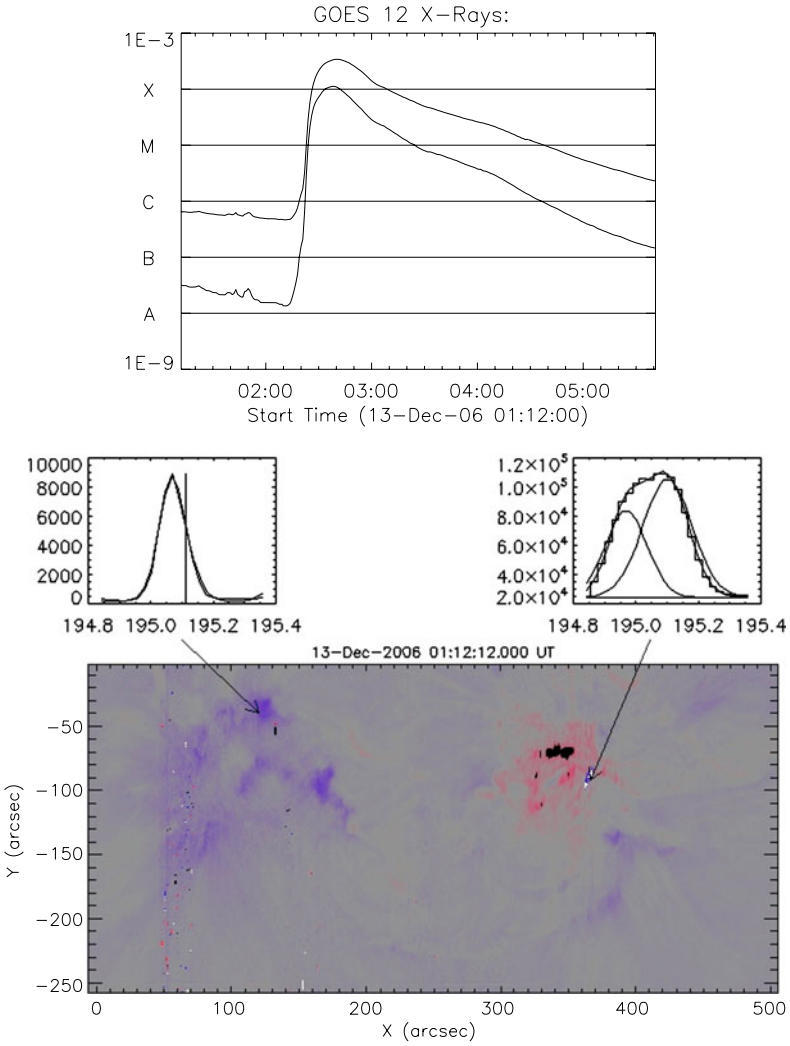

Figure 3 The top plot shows the GOES light curve from the start of the EIS raster to the end of the raster. The line profiles of Fe XII are shown in the dimming region (to the left) and the filament eruption (to the right). Arrows highlight a pixel in the dimming region (at 04:33 UT) and a pixel in the filament region (02:23 UT). The dimming region shows symmetric line profiles, whereas the filament eruption also shows strong blue-shifted plasma. The bottom image shows the Doppler velocity image from the EIS. Time in this case goes from right to left.

corrected for solar rotation to the time of the pre-flare raster. When compared to the intensity difference image, the strong velocities do not cover the entire dimming region. This allows us to focus on the regions from which the fastest plasma, which is most likely to become part of the ICME, originates. Use of the velocity difference allowed us to determine the magnetic flux of all the regions showing strong velocity enhancements due to the flare and eruption. The magnetic flux in maxwell (Mx) for the region with velocity enhancement is determined to be 3.8×10^{21} Mx (positive) and 7.1×10^{20} Mx (negative) for the whole region observed by the EIS. The magnetic fluxes of the plage region and the core of the AR were

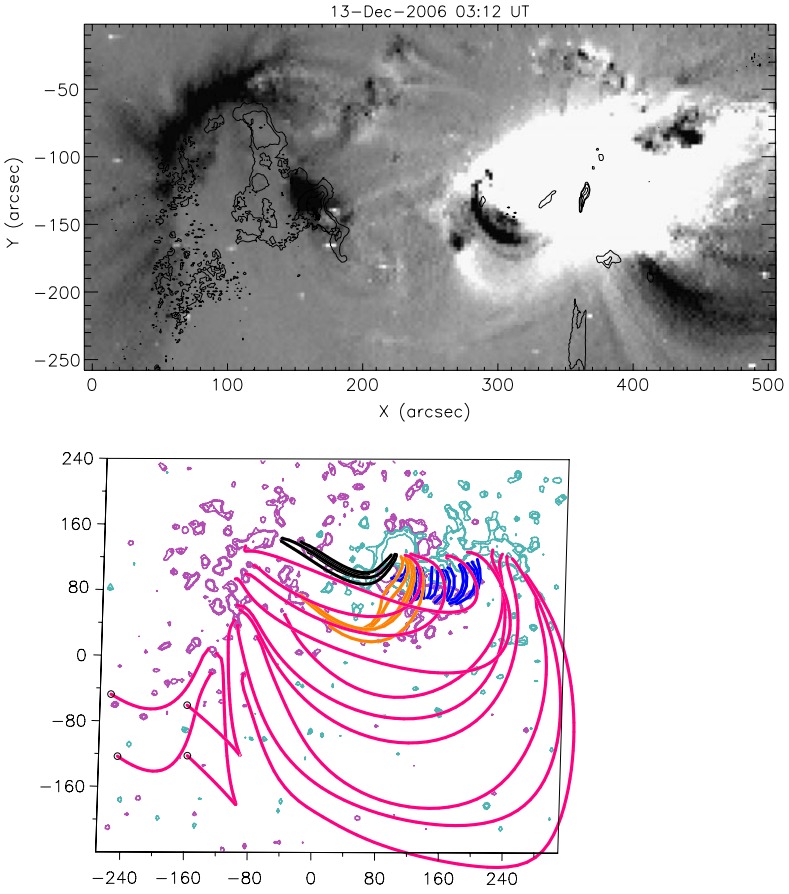

Figure 4 (Top) EIT 195 Å difference image where white shows enhanced intensity and dark shows reduced intensity. The pre-event image on 13 December 2006 at 00:00 UT was subtracted from this image. The black contours show the blue-shifted Doppler velocities with levels ranging from -20 km s^{-1} to -100 km s^{-1}. (Bottom) Coronal magnetic field model showing the field connectivity along the main AR PIL. The field lines have been computed at increasingly farther distances from the PIL and with different values for the linear force-free parameter α, with blue showing the highest value of α, orange the intermediate α, and red the lower value of α. The field lines drawn in black match the shape of the sigmoid observed in XRT images before the flare. See text for further details. Blue (purple) contours highlight the negative (positive) magnetic field contours (± 50, ± 100, and ± 500 G).

also determined by selecting sub-regions of the map. We assumed a 20 G magnetic field threshold to account for the small closed magnetic loops in the quiet Sun.

There are two errors in the magnetic flux. The first is the error in the magnetic field threshold to account for the closed quiet Sun loops. We assumed a value of 20 G. If we increase that to 25 G, then the flux values decrease by around 1 – 2%. The larger error is the value chosen for the velocity enhancement. We determined values for 10 km s^{-1} and 20 km s^{-1} for the whole region, the plage region only, and the AR core only. These are shown in Tables 1 and 2. The increase to a velocity difference of 10 to 20 km s^{-1} decreases the magnetic flux values by between 30% to 80% with the largest change occurring in the AR core. This is not surprising, as the AR core contains the strongest magnetic field and

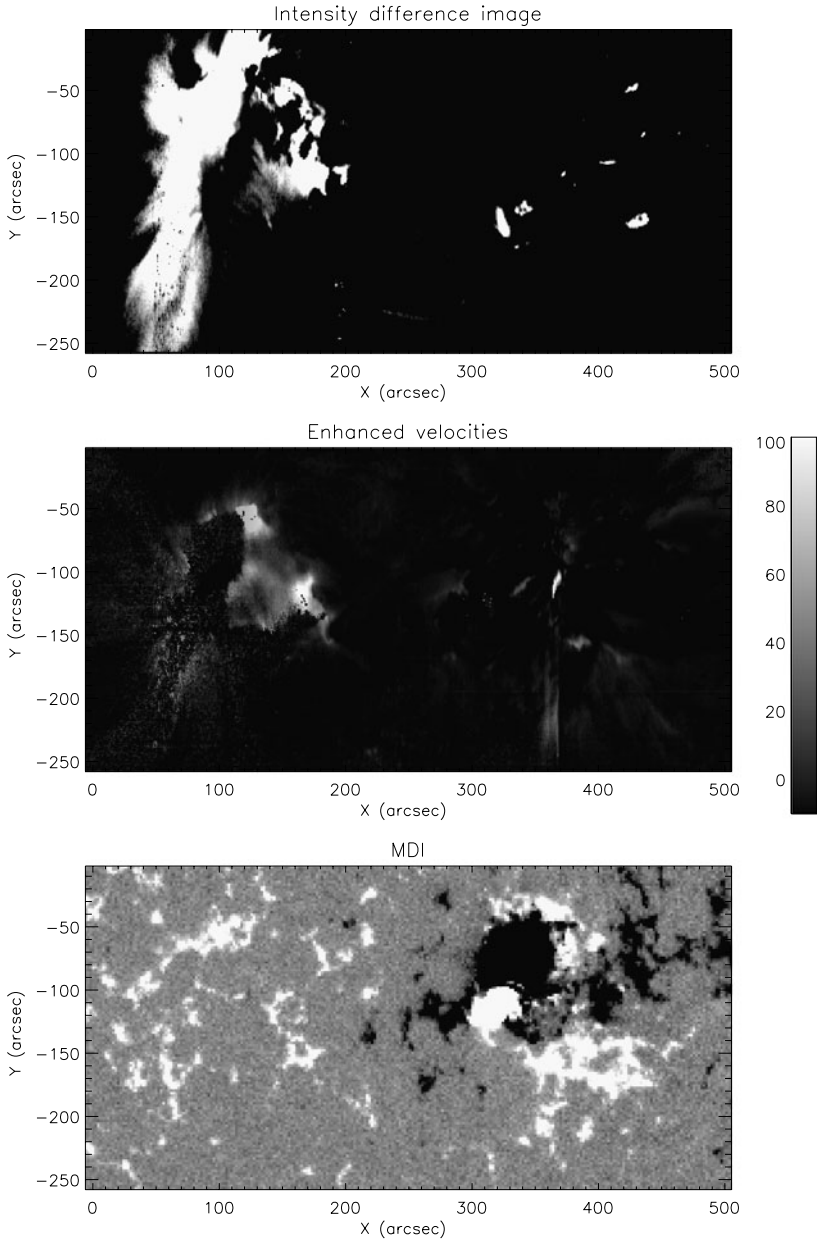

Figure 5 The top figure shows the intensity difference between the EIS raster on 12 December 2006 at 19:07 UT and the next raster on 13 December 2006 at 01:12 UT. The middle figure shows the velocity difference between the EIS raster on 12 December 2006 at 19:07 UT and the next raster on 13 December 2006 at 01:12 UT. The colour bar shows the velocity difference magnitude. Only the enhanced blue shifts are shown. The lower figure shows the MDI data on 12 December 2006 at 19:15 UT.

Table 1 Magnetic flux in different regions for a velocity difference of 10 km s^{-1}.

Region	+ flux (Mx)	− flux (Mx)
Whole region	3.8×10^{21}	-7.1×10^{20}
Plage	2.6×10^{21}	-7.6×10^{18}
Core AR	5.9×10^{20}	-6.3×10^{20}

Table 2 Magnetic flux in different regions for a velocity difference of 20 km s^{-1}.

Region	+ flux (Mx)	− flux (Mx)
Whole region	1.9×10^{21}	-1.3×10^{20}
Plage	1.3×10^{21}	-5.5×10^{18}
Core AR	3.8×10^{20}	-1.3×10^{20}

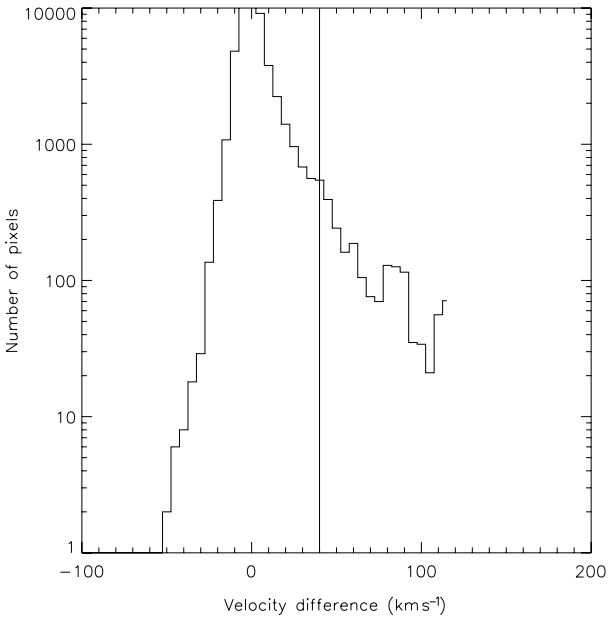

Figure 6 A histogram of the velocity difference values between the pre-flare velocities and the flare velocities. The positive values show an enhancement in the blue-shifted speeds. The solid vertical line shows the lower limit of the velocity enhancement for the filament eruption.

the largest outflows. Figure 6 shows a histogram of the range of the magnitude of velocity differences. The largest numbers of pixels are in the region with velocity difference between -10 and $+30$ km s^{-1}, so a change in the threshold around these values will produce large changes in the magnetic flux magnitude, as has been shown in the tables.

3.2. The Origin of the Remote Dimmings

In this section we investigate the origin of the remote dimming located to the east of the AR on a large plage region. In principle, one may argue that due to its location, far from the source AR, this dimmed region has no relation to the footprint of the CME. In large-scale events occurring in very complex ARs, dimmings are distributed on the solar surface in a more complicated way than that in simple bipolar regions, as discussed in Section 1.

Secondary dimmings can develop far from the initial CME source region at remote locations and, in principle, their connection to the ejection is not as clear as in the case of core dimmings. However, their long lifetimes (several hours) and mapping to the CME cavity (see *e.g.* Attrill *et al.*, 2009; Chen, 2009) suggest that they are also due to plasma evacuation. The plasma can be evacuated either because of the direct expansion of the magnetic field, which is anchored to the secondary dimming region, or because magnetic reconnection occurs between the laterally expanding CME field and the surrounding magnetic field structures (Attrill *et al.*, 2007; Mandrini *et al.*, 2007; Cohen *et al.*, 2009) (see also the discussion in van Driel-Gesztelyi *et al.* (2008) on the relevance of the surrounding magnetic field topology for the development of CME low coronal signatures). In essence, the existence of secondary dimmings depends on the large-scale connectivity that develops dynamically during the CME by itself or between the CME and the surrounding field.

We have modelled the AR magnetic field using a linear force-free model ($\nabla \times \mathbf{B} = \alpha \mathbf{B}$, with α a constant), and we have explored the field connectivity along the main AR polarity inversion line (PIL). For this model, we have used as a boundary condition the MDI magnetogram at 03:15 UT on 13 December.

During the flare, loops are hardly distinguishable in EUV or soft X-rays because of significant image saturation. An inverse sigmoidal shape is clearly visible to the east of the main AR spot in XRT images obtained on the day previous to the flare (12 December 2006 at 19:01 UT; see also Figure 8 in Attrill *et al.* (2010)), indicating that the AR magnetic helicity is negative. This sigmoidal set of loops becomes visible again after the flare on 13 December in EIT images at $\approx$ 06:18 UT, showing a global magnetic AR restructuring after the event. Using the method discussed in Green *et al.* (2002), we find that the value of α that best matches those loops is -7.5×10^{-2} Mm^{-1} (see the set of black field lines in the lower panel of Figure 4); however, at the flare time the magnetic field shear is probably larger. Starting from the high value of α, we computed field lines by reducing the absolute value of α for each computation. The footpoints of these field lines are chosen at increasing distances from the PIL on the main negative AR spot. Figure 4 (bottom) shows the computed field lines; the ones in blue (computed for $\alpha = -7.5 \times 10^{-2}$ Mm^{-1}) correspond to the arcade overlying the PIL that will first expand and reconnect as the flare/CME evolves. This lower-lying arcade will be replaced by an arcade of reconnected loops formed at the first stages of the flare evolution and visible in the EIT image on 13 December at 03:24 UT. The field lines in orange ($\alpha = -6.3 \times 10^{-2}$ Mm^{-1}) correspond to the arcade at a later time, and the ones in red ($\alpha = -3.1 \times 10^{-2}$ Mm^{-1}) to a still later time. The progression of the field lines in height somewhat resembles the flare temporal evolution, from a more sheared (close to the neutral line) to a less sheared field as the flare evolves and the ribbons separate from the inversion line. The magnetic field configuration will be restructured through a series of expansions and reconnections in this process. The location of the footpoints of the arcade field lines (on the positive field) shift from the main AR positive polarity towards the positive polarity of the plage region to the east, where the secondary dimming region is located.

As shown in Figure 4, the location of the positive footpoints of the overlying arcade field lines shifts from the main AR positive polarity towards the positive polarity of the plage region to the east, where the secondary dimming region is located. This evolution suggests that the loops anchored at the secondary dimming first expand and then reconnect at large heights in the corona. As these new and extended connectivities are established, the plasma fills a larger volume, resulting in reduced intensity of the loops. Thus, the existence of the outflows in the plage region and the secondary dimmings is a consequence of the expansion and connectivity evolution that develops during the flare/CME. This eruption is unusual in that the plage region becomes so intimately connected to the AR.

Attrill *et al.* (2010) studied the recovery of the dimmings after the CMEs on 13 and 14 December 2006 and concluded that the concentrated outflows at the secondary dimming region are located at the footpoints of coronal loops that exist before and are re-established after the eruptions. From the Attrill *et al.* (2010) results and ours, we speculate that after the flare, and for as long as the secondary dimmings are visible, the loops that extend from the positive field in the plage region towards the south (see the small negative polarities in Figure 4 and the EIS image at 19:07 UT on 12 December 2006) and exist before the event are somehow "obscured" by the new large-scale connectivities established by the flare/CME expansion. After the event and when the plasma in the progressively larger expanding loops is no longer visible in EIT wavebands, the previously existing loops can be observed again (see Figure 3 in Attrill *et al.* (2010) on 14 December at 07:03 UT).

From this discussion, we conclude that the magnetic flux in the secondary dimming region is related to the ejection and must be added to the flux in the core dimming region, found using the new method discussed in Section 3.1.

3.3. The Magnetic Flux in the Coronal Mass Ejection

It is noticeable from Tables 1 and 2 that the magnetic flux computed using both velocity enhancement thresholds is almost balanced in the core region, but not in the plage region where there are three orders of magnitude difference between the positive and the negative fluxes.

Following Mandrini *et al.* (2007), and considering the two extreme cases for the formation of dimming regions discussed by these authors (see also Section 3.2) and their relation to the ejected magnetic flux, we would expect similar values for the positive and negative flux both in the core and plage regions. If this were the case, then the magnetic flux involved in the ejection could have been estimated as the average between the positive and negative fluxes (after adding the core to the plage magnetic flux, see Section 3.2).

As shown in Figures 4 and 5 the strongest polarities in the plage region are positive. These positive polarities are, on one hand, connected to very low intensity negative diffuse polarities towards the south (as discussed in Section 3.2). On the other hand, and as shown in Section 3.2 (see Figure 4), large-scale connectivities exist to negative polarities far outside our region of interest and to the main negative polarity of AR 10930. This is also apparent in Figure 8 of Attrill *et al.* (2010), which clearly shows the large-scale structure emanating from the plage region. Since our method is based on computing velocity enhancements using spectroscopic data, we do not include those regions outside the EIS field of view or those for which the magnetic field intensity is below our 20 G threshold. Furthermore, it might be expected that since the AR main negative polarity partially connects to the positive polarity in the plage region, the negative magnetic flux associated to the velocity enhancements in the core should be higher to compensate the flux unbalance in the plage region, but this is not the case. A plausible reason for this is the clear saturation of MDI data at the location of the main negative spot, which results in pixels having much lower magnetic field intensity than expected when compared to their non-saturated neighbours (see the discussion in Green *et al.* (2003)).

Taking these factors into consideration, we conclude that the magnetic flux involved in the ejection is best represented by the positive flux values adding the core to plage flux. Since there is no reason to prefer either velocity threshold, we conclude that the magnetic flux in the ejected plasma would be in the range $[2-4] \times 10^{21}$ Mx.

4. The Interplanetary Flux Rope

4.1. Magnetic Cloud Model and Flux Determination

In this section we analyse the interplanetary manifestation of the CME ejected on 13 December 2006. At 1 AU, the ejected plasma was observed as a left-handed MC (Liu *et al.*, 2008). We model its magnetic structure using *in situ* observations and compute its magnetic flux to compare it with the one inferred from solar data in Section 3.

Liu *et al.* (2008) have identified the start and end times for this MC; in particular, they define the cloud extent from 22:48 UT on 14 December to 04:34 UT on 15 December. From an analysis of magnetic field and plasma observations, and looking for typical cloud properties (*e.g.* coherent rotation of **B**, high values of the magnetic field intensity (B), low values of the proton plasma β parameter, proton temperature lower than expected at the observed bulk velocity, current sheets at the boundaries due to magnetic connectivity changes) that let us distinguish it from other interplanetary structures, we choose MC boundaries starting at 23:15 UT on 14 December and ending at 05:15 UT on 15 December. Several sub-intervals showing non-typical alpha-particle abundances are present within this range. Our selection for the MC boundaries is very similar to that of Liu *et al.* (2008).

To give the cloud axis direction in the GSE system, we define the latitude angle (θ) between the ecliptic plane and the cloud axis, and the longitude angle (ϕ) between the projection of the axis on the ecliptic plane and the Earth – Sun direction measured counterclockwise.

A reference frame oriented in the same direction as the flux rope is useful to analyse the magnetic vector time series observed by the spacecraft. This allows us to identify magnetic features inside the flux rope and to improve the determination of its boundaries. The base of this 'local' system of coordinates (see *e.g.* Dasso *et al.*, 2009) considers $z_{\rm MC}$ pointing along the cloud axis (with $B_{z,\rm MC} > 0$ at the flux rope axis), $x_{\rm MC}$ as the direction given by the rectilinear trajectory of the spacecraft projected on the plane perpendicular to $z_{\rm MC}$, and $y_{\rm MC}$ such that ($x_{\rm MC}$, $y_{\rm MC}$, $z_{\rm MC}$) form a right-handed system. We also define the impact parameter, p, as the minimum approach distance from the spacecraft to the cloud axis.

We model the observed magnetic field using the classical cylindrical linear force-field model (Lundquist, 1950). In this model the field is described by

$$\mathbf{B}_{\rm L} = B_0\big[J_1(\alpha r)\,\hat{\phi} + J_0(\alpha r)\,\hat{\mathbf{z}}\big], \tag{1}$$

where J_n is the Bessel function of the first kind of order n, B_0 is the strength of the field at the MC axis, and α is a constant, linked to the local twist of field lines as in the solar case.

From this model and for a cylindrical magnetic configuration with radius R and axial length L, the axial magnetic flux is given by $F_z = 2\pi B_0 R J_1(\alpha R)/\alpha$, and the azimuthal magnetic flux is given by $F_\phi = L B_0\,(1 - J_0(\alpha R))/\alpha$.

We compare the proposed model with the *in situ* observed magnetic field (see *e.g.* Dasso *et al.*, 2003; Gulisano *et al.*, 2005) and determine the free parameters of the model (physical parameters, B_0 and α, and geometrical parameters, p, θ, and ϕ), minimising the difference between the model predictions and the observations. Since both the geometrical and physical parameters are fitted simultaneously, we call our method the *Simultaneous Fit* (SF). Applying the SF, we obtain $\theta = -49°$ and $\phi = 64°$ for the flux rope orientation, a negligible impact parameter, $B_0 = 18.8$ nT, and $\alpha = -15.8$ AU^{-1}.

From the fitted values of B_0 and α, and the expressions given above, we compute the magnetic fluxes and obtain $F_z = 3.8 \times 10^{20}$ Mx and $F_\phi/L = 5.1 \times 10^{20}$ Mx AU^{-1}.

We rotate the observed magnetic field vectors to the orientation obtained from the SF method; thus, we find the time series of the field components in this MC frame. Figure 7 shows several features that support the existence of an MC in agreement with the time range we selected. The three upper panels show the components of **B** in the cloud frame, and the lower panels show the bulk speed and the proton temperature, for an extended range around the MC. The three components of **B** show the typical shape of a magnetic flux rope. The almost constant and near to zero $B_{x,\mathrm{MC}}$ values indicate that p is low for this cloud, in agreement with the SF. The time profile of $B_{y,\mathrm{MC}}$ shows the coherent rotation of the azimuthal magnetic field, from positive at the beginning to negative at the end, passing through zero at the centre. The shape of $B_{z,\mathrm{MC}}$ is qualitatively as expected, lower near the boundaries and maximum close to the cloud centre, though its profile is quite flat. This flat profile is not always present in clouds, but it has been observed in several other events (*e.g.*, Dasso *et al.*, 2006).

Magnetic clouds are expected to be in expansion during their travel from the Sun because of the global decay of the total solar wind pressure (Gulisano *et al.*, 2010). The bulk speed for this cloud is in agreement with an expanding MC, travelling faster in the front than in the back. The observed proton temperature is lower than expected (T_{ex}) for a typical solar wind at a given observed bulk velocity (Lopez, 1987; Démoulin, 2009), in agreement with typical observations of an MC (Richardson and Cane, 1995).

When the MC local frame is well determined, and for a general shape of the MC cross section, one expects to find that (Dasso *et al.*, 2006)

$$\int_{\text{flux rope}} B_{y,\mathrm{MC}}\,\mathrm{d}x = 0. \tag{2}$$

The second panel from the top of Figure 7 shows the cumulative azimuthal flux F_y (red line superimposed on $B_{y,\mathrm{MC}}$) calculated from the MC start time X_{in} using the expression:

$$\frac{F_y(x)}{L} = \int_{X_{\mathrm{in}}}^{x} B_{y,\mathrm{MC}}(x')\,\mathrm{d}x', \tag{3}$$

which shows that F_y cancels within $\approx 15\%$ at the place chosen as the end of the flux rope. This lack of exact cancellation is probably due to uncertainties in the exact orientation of the flux rope. This result further stresses the importance of accurate determination of the boundaries and also provides an estimation of the time associated with the cloud centre from the minimum value of F_y, which is at 02:15 UT on 15 December.

As shown in Figure 7, the profile of $B_{y,\mathrm{MC}}$ is rather peculiar; therefore, to obtain more precise MC flux values and determine their error bars, we explore different orientations for the flux rope (θ is varied between $-40°$ and $-70°$, and ϕ between $60°$ and $90°$), and we use a method of analysis that separates the time range covered by the cloud into two branches (the inbound/outbound branches; see *e.g.* Dasso *et al.* (2005) and Attrill *et al.* (2006)) and fits each branch in a separate way. This process gives us the following averaged values for the fluxes: $F_z = (4.6 \pm 0.8) \times 10^{20}$ Mx and $F_\phi/L = (6.0 \pm 0.9) \times 10^{20}$ Mx AU^{-1}, where the uncertainties were computed as the standard deviations from all the different methods and orientations explored.

In order to determine the azimuthal or poloidal MC flux, we need an estimation for the cloud length. Analysing observations of suprathermal electrons from the Solar Wind Electron Analyzer (SWEA, Sauvaud *et al.*, 2008) on board the *Solar Terrestrial Relations Observatory* A (STEREO A), Liu *et al.* (2008) found the presence of counter-streaming electron flows within the MC. This would imply that the cloud is anchored to the Sun at

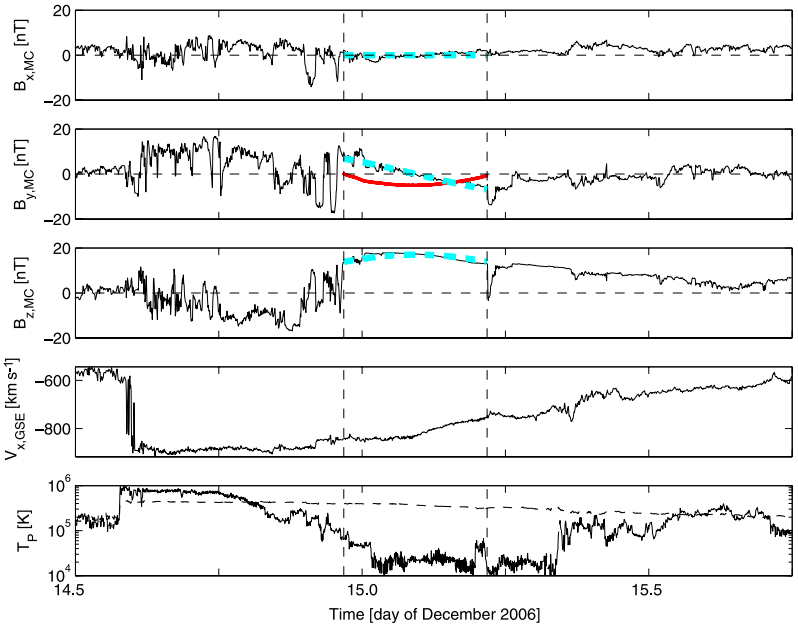

Figure 7 The three components of the magnetic field in the cloud frame $B_{x,\mathrm{MC}}$, $B_{y,\mathrm{MC}}$, and $B_{z,\mathrm{MC}}$ are shown in the first three panels from top to bottom; in the second panel we superimpose the magnetic flux F_y (see main text) in arbitrary units (red line). The light blue dashed lines correspond to the fitted Lundquist model. In the fourth panel, we show the solar wind velocity in the $\mathrm{x_{GSE}}$ direction, and in the last panel we plot the observed (solid line) and expected (dashed line) proton temperatures as a function of time. The MC boundaries are marked with vertical dashed lines.

both ends when observed at 1 AU; thus, the MC length should be at least 2 AU. We can either consider this minimum length or, following the results of Larson *et al.* (1997), take a length of ≈ 2.5 AU, which is more realistic; then $F_\phi \approx (1.5 \pm 0.2) \times 10^{21}$ Mx.

4.2. The Relation Between the Ejected and Magnetic Cloud Fluxes

In principle the fluxes in both cloud components (axial and azimuthal) compare to the flux involved in the ejection at the solar level depending on how the ejection initiates. As discussed in Mandrini *et al.* (2007), 'two extreme cases can be considered for the CME initiation. In the first case, a flux rope could be present before an eruption, or it could be formed by magnetic reconnection of a sheared arcade before any significant expansion of the magnetic configuration occurs. In this case, dimmings would be formed only at the footpoints of the flux tube as it expands and erupts. Then, the flux measured in the dimmings would be comparable mainly to the MC axial flux. In the second case, the arcade above the flux rope could expand significantly before reconnecting (as in the theoretical two-dimensional model for flux rope expansion by Lin and Forbes (2000)). Then, the dimmings would be formed at the footpoints of the flux rope, and also all along the footpoints of the sheared magnetic arcade as this expansion occurs. Later, the reconnection of the sheared arcade field lines would progressively incorporate more flux to the erupting flux tube. In this second case, the flux in the dimming regions would be comparable to the sum of the axial and azimuthal MC flux. In

view of this discussion, we sum F_z and F_ϕ and call this value $F_{\rm MC} \approx (2.0 \pm 0.3) \times 10^{21}$ Mx. This is the number that should be compared to the ejected coronal flux determined in Section 3.

5. Discussion

It is important, yet difficult, to link the plasma ejected from the Sun to that measured in coronagraph data and harder still to link it to the plasma measured in ICMEs using *in situ* data. Comparisons between solar sources and white-light data (e.g. Sterling and Hudson, 1997; Jin *et al.*, 2009) have found that the mass loss determined from the dimming regions was smaller than that derived from white-light observations. It is difficult to measure the dimming regions in the flaring AR itself as it is usually dominated by flaring emission, and this is a weakness in the coronal 'dimming' method. In this paper we attempt a new technique for measuring the source of a CME using a velocity difference technique. This allows the measurement of any strongly outflowing plasma from the region, regardless of the brightness. The example shown is the 13 December 2006 X class flare. In this case both dimming regions and the flaring region were observed spectroscopically. This allowed us to use the pre-flare and post-flare data to look at regions that had enhanced velocity. We checked that the remote dimming region could be related to the CME by carrying out magnetic field modelling of the AR and its surroundings. From that model it is clear that, as the flare/CME progresses, this nearby plage region is involved in the eruption. From this information, we then include outflowing material from both the core and dimming regions.

The magnetic flux at the interplanetary medium turned out to be $(2.0 \pm 0.3) \times 10^{21}$ Mx, and the magnetic flux from the source of the CME, determined by the velocity difference method, was $[2.0 - 4.0] \times 10^{21}$ Mx. Though the first value is closer to the lower limit for the flux in the ejected plasma, these values are in good agreement, suggesting that the methodology works well. There are two reasons why this method differs from that using simply the intensity difference method. First, the dimming regions with the strongest outflow can be extracted. A comparison of the intensity and velocity differences images shown in Figure 5 illustrates a clear difference in the structure of the main dimming region. The area showing strong velocity is much smaller than that showing a strong intensity decrease. Second, the intensity difference method does not allow the detection of a dimming region in the core AR due to the brightness of the flare. However, the velocity difference method can detect the strong upflows associated with the eruption in the core active region. In this particular case, the magnetic flux determined from the core of the AR is small, and the dominant flux is from the dimming in the plage region. But this case is unusual due to the intimate link between the plage region and the AR, as illustrated in Figure 4. We expect that in other cases the outflow region in the core AR will provide more significant magnetic flux. Indeed, in this large AR we also had an issue with the magnetic field saturation in the MDI data.

Note also that the magnetic flux in the axial cloud component ($F_z = (4.6 \pm 0.8) \times 10^{20}$ Mx) is around three times lower than the flux in the azimuthal component ($F_\phi = (1.5 \pm 0.2) \times 10^{21}$ Mx), when we consider a cloud length (one of the unknowns when modelling an MC magnetic configuration) compatible with SWEA observations. Furthermore, the magnetic flux in the azimuthal field component is the closest to the flux estimated to be involved in the solar ejection. This result is similar to those found in other studies (Mandrini *et al.*, 2005; Attrill *et al.*, 2006; Qiu *et al.*, 2007) and suggests that the ejected flux rope was mostly formed by magnetic reconnection during the eruption process.

In conclusion, the velocity difference method produces magnetic fluxes in agreement with the MC flux. However, we made an assumption for the velocity difference value (10

and 20 km s^{-1}), and we found compatible fluxes both at the Sun and in the interplanetary medium, with the MC flux closer to the lower limit for the flux in the ejection (which corresponds to a velocity difference of 20 km s^{-1}). We have no justification for using these particular values, and a wide range of velocity difference values exist (see Figure 6). To refine this method, we need to determine a physical reason for choosing the velocity difference value and make detailed comparisons with CME models.

The Hinode EIS data allows us a new way of viewing the CME source which, in this work, has proven to be invaluable in understanding the source of an ICME.

Acknowledgements Hinode is a Japanese mission developed and launched by ISAS/JAXA, collaborating with NAOJ as a domestic partner and NASA and STFC (UK) as international partners. Scientific operation of the Hinode mission is conducted by the Hinode science team organised at ISAS/JAXA. This team mainly consists of scientists from institutes in the partner countries. Support for the post-launch operation is provided by JAXA and NAOJ (Japan), STFC (UK), NASA (USA), ESA, and NSC (Norway). We thank the ACE SWEPAM instrument team and the ACE Science centre for providing the ACE data. We thank the Royal Society for a travel fund award. C.H.M. acknowledges financial support from the Argentinean grants UBACyT X127, PIP 2009-100766 (CONICET), and PICT 2007-1790 (ANPCyT). S.D. and A.M.G. express thanks for the Argentinean grants UBACyT 20020090100264, PICT 00856 (ANPCyT), and PIP 2009-00825 (CONICET). C.H.M. and S.D. are members of the Carrera del Investigador Científico (CONICET). K.S. thanks STFC for support via a Ph.D. studentship.

References

Asai, A., Hara, H., Watanabe, T., Imada, S., Sakao, T., Narukage, N., Culhane, J.L., Doschek, G.A.: 2008, *Astrophys. J.* **685**, 622.
Attrill, G.D.R., Harra, L.K., van Driel-Gesztelyi, L., Démoulin, P.: 2007, *Astrophys. J. Lett.* **656**, 101.
Attrill, G.D.R., Engell, A.J., Wills-Davey, M.J., Grigis, P., Testa, P.: 2009, *Astrophys. J.* **704**, 1296.
Attrill, G.D.R., Harra, L.K., van Driel-Gesztelyi, L., Wills-Davey, M.J.: 2010, *Solar Phys.* **264**, 119.
Attrill, G., Nakwacki, M.S., Harra, L.K., van Driel-Gesztelyi, L., Mandrini, C.H., Dasso, S., Wang, J.: 2006, *Solar Phys.* **238**, 117.
Chen, P.F.: 2009, *Astrophys. J. Lett.* **698**, 112.
Cohen, O., Attrill, G.D.R., Manchester, W.B., Wills-Davey, M.J.: 2009, *Astrophys. J.* **705**, 587.
Crooker, N.U., Webb, D.F.: 2006, *J. Geophys. Res.* **111**, 8108.
Culhane, J.L., Harra, L.K., James, A.M., Al-Janabi, K., Bradley, L.J., Chaudry, R.A., *et al.*: 2007, *Solar Phys.* **243**, 19.
Dasso, S., Mandrini, C.H., Démoulin, P., Farrugia, C.J.: 2003, *J. Geophys. Res.* **108**, 1362.
Dasso, S., Mandrini, C.H., Démoulin, P., Luoni, M.L.: 2006, *Astron. Astrophys.* **455**, 349.
Dasso, S., Mandrini, C.H., Schmieder, B., Cremades, H., Cid, C., Cerrato, Y., *et al.*: 2009, *J. Geophys. Res.* **114**, 2109.
Delaboudinière, J., Artzner, G.E., Brunaud, J., Gabriel, A.H., Hochedez, J.F., Millier, F., *et al.*: 1995, *Solar Phys.* **162**, 291.
Démoulin, P.: 2009, *Solar Phys.* **257**, 169.
Freeland, S.L., Handy, B.N.: 1998, *Solar Phys.* **182**, 497.
Golub, L., Deluca, E., Austin, G., Bookbinder, J., Caldwell, D., Cheimets, P., *et al.*: 2007, *Solar Phys.* **243**, 63.
Green, L.M., López Fuentes, M.C., Mandrini, C.H., Démoulin, P., Van Driel-Gesztelyi, L., Culhane, J.L.: 2002, *Solar Phys.* **208**, 43.
Green, L.M., Démoulin, P., Mandrini, C.H., Van Driel-Gesztelyi, L.: 2003, *Solar Phys.* **215**, 307.
Gulisano, A.M., Dasso, S., Mandrini, C.H., Démoulin, P.: 2005, *J. Atmos. Solar-Terr. Phys.* **67**, 1761.
Gulisano, A.M., Démoulin, P., Dasso, S., Ruiz, M.E., Marsch, E.: 2010, *Astron. Astrophys.* **509**, A39.
Handy, B.N., Acton, L.W., Kankelborg, C.C., Wolfson, C.J., Akin, D.J., Bruner, M.E., *et al.*: 1999, *Solar Phys.* **187**, 229.
Harra, L.K., Hara, H., Imada, S., Young, P.R., Williams, D.R., Sterling, A.C., Korendyke, C., Attrill, G.D.R.: 2007, *Publ. Astron. Soc. Japan* **59**, 801.
Harrison, R.A., Lyons, M.: 2000, *Astron. Astrophys.* **358**, 1097.
Hudson, H.S., Cliver, E.W.: 2001, *J. Geophys. Res.* **106**, 25199.
Hudson, H.S., Acton, L.W., Freeland, S.L.: 1996, *Astrophys. J.* **470**, 629.

Imada, S., Hara, H., Watanabe, T., Kamio, S., Asai, A., Matsuzaki, K., Harra, L.K., Mariska, J.T.: 2007, *Publ. Astron. Soc. Japan* **59**, 793.
Jin, M., Ding, M.D., Chen, P.F., Fang, C., Imada, S.: 2009, *Astrophys. J.* **702**, 27.
Larson, D.E., Lin, R.P., McTiernan, J.M., McFadden, J.P., Ergun, R.E., McCarthy, M., *et al.*: 1997, *Geophys. Res. Lett.* **24**, 1911.
Lin, J., Forbes, T.G.: 2000, *J. Geophys. Res.* **105**, 2375.
Liu, Y., Luhmann, J.G., Müller-Mellin, R., Schroeder, P.C., Wang, L., Lin, R.P., Bale, S.D., Li, Y., Acuña, M.H., Sauvaud, J.: 2008, *Astrophys. J.* **689**, 563.
Longcope, D., Beveridge, C., Qiu, J., Ravindra, B., Barnes, G., Dasso, S.: 2007, *Solar Phys.* **244**, 45.
Lopez, R.E.: 1987, *J. Geophys. Res.* **92**, 11189.
Lundquist, S.: 1950, *Ark. Fys.* **2**, 361.
Mandrini, C.H.: 2010, In: Kosovichev, A.G., Andrei, A.H., Rozelot, J.-P. (eds.) *Solar and Stellar Variability: Impact on Earth and Planets, IAU Symp.*, **264**, 257.
Mandrini, C.H., Pohjolainen, S., Dasso, S., Green, L.M., Démoulin, P., van Driel-Gesztelyi, L., Copperwheat, C., Foley, C.: 2005, *Astron. Astrophys.* **434**, 725.
Mandrini, C.H., Nakwacki, M.S., Attrill, G., van Driel-Gesztelyi, L., Démoulin, P., Dasso, S., Elliott, H.: 2007, *Solar Phys.* **244**, 25.
Mandrini, C.H., Nakwacki, M.S., Attrill, G., van Driel-Gesztelyi, L., Dasso, S., Démoulin, P.: 2009, In: Gopalswamy, N., Webb, D.F. (eds.) *Universal Heliophysical Processes*, *IAU Symp.* **257**, 265.
McComas, D.J., Bame, S.J., Barker, P., Feldman, W.C., Phillips, J.L., Riley, P., Griffee, J.W.: 1998, *Space Sci. Rev.* **86**, 563.
Möstl, C., Miklenic, C., Farrugia, C.J., Temmer, M., Veronig, A., Galvin, A.B., Vršnak, B., Biernat, H.K.: 2008, *Ann. Geophys.* **26**, 3139.
Ogilvie, K.W., Desch, M.D.: 1997, *Adv. Space Res.* **20**, 559.
Qiu, J., Hu, Q., Howard, T.A., Yurchyshyn, V.B.: 2007, *Astrophys. J.* **659**, 758.
Reinard, A.A., Biesecker, D.A.: 2009, *Astrophys. J.* **705**, 914.
Richardson, I.G., Cane, H.V.: 1995, *J. Geophys. Res.* **100**, 23397.
Rust, D.M.: 1983, *Space Sci. Rev.* **34**, 21.
Sauvaud, J., Larson, D., Aoustin, C., Curtis, D., Médale, J., Fedorov, A., *et al.*: 2008, *Space Sci. Rev.* **136**, 227.
Scherrer, P.H., Bogart, R.S., Bush, R.I., Hoeksema, J.T., Kosovichev, A.G., Schou, J., *et al.*: 1995, *Solar Phys.* **162**, 129.
Smith, C.W., L'Heureux, J., Ness, N.F., Acuña, M.H., Burlaga, L.F., Scheifele, J.: 1998, *Space Sci. Rev.* **86**, 613.
Sterling, A.C., Hudson, H.S.: 1997, *Astrophys. J. Lett.* **491**, 55.
Stone, E.C., Frandsen, A.M., Mewaldt, R.A., Christian, E.R., Margolies, D., Ormes, J.F., Snow, F.: 1998, *Space Sci. Rev.* **86**, 1.
Thompson, B.J., Plunkett, S.P., Gurman, J.B., Newmark, J.S., St. Cyr, O.C., Michels, D.J.: 1998, *Geophys. Res. Lett.* **25**, 2465.
van Driel-Gesztelyi, L., Attrill, G.D.R., Démoulin, P., Mandrini, C.H., Harra, L.K.: 2008, *Ann. Geophys.* **26**, 3077.
Webb, D.F., Lepping, R.P., Burlaga, L.F., DeForest, C.E., Larson, D.E., Martin, S.F., Plunkett, S.P., Rust, D.M.: 2000, *J. Geophys. Res.* **105**, 27251.
Williams, D.R., Harra, L.K., Brooks, D.H., Imada, S., Hansteen, V.H.: 2009, *Publ. Astron. Soc. Japan* **61**, 493.
Zhukov, A.N., Auchère, F.: 2004, *Astron. Astrophys.* **427**, 705.